# Theoretical Study on Molecules of Interstellar Interest. II. Radical Cation of Compact Polycyclic Aromatic Hydrocarbons

Samala Nagaprasad Reddy and S. Mahapatra*

School of Chemistry, University of Hyderabad, Hyderabad 500046, India

S *Supporting Information*

ABSTRACT: Radical cations of polycyclic aromatic hydrocarbons have been postulated to be molecular carriers of diffuse spectroscopic features observed in the interstellar medium. Several important observations made by stellar and laboratory spectroscopists motivated us to undertake a detailed theoretical study attempting to validate the recorded data. In continuation of our work on this subject, we here focus on a detailed theoretical study of the doublet ground ($\tilde{X}$) and low-lying excited ($\tilde{A}$, $\tilde{B}$, and $\tilde{C}$) electronic states of the radical cation of phenanthrene, pyrene, and acenaphthene molecule. A multistate and multimode theoretical model in a diabatic electronic basis is developed here through extensive ab initio quantum chemistry calculations. Employing this model, first-principles nuclear dynamics calculations are carried out to unravel the spectral assignment, time-dependent dynamics, and photostability of the mentioned electronic states of the radical cations. The theoretical results compare well with the observed experimental data.

Polycyclic aromatic hydrocarbons of interstellar interest
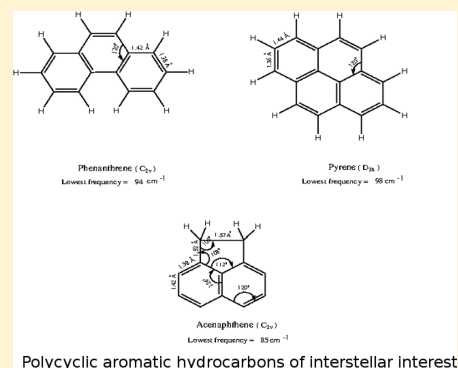
I. INTRODUCTION

Diffuse interstellar bands (DIBs) are a set of ubiquitous absorption features observed from ground telescopes throughout the near-infrared and visible region of the electromagnetic spectrum. The first observation of the two strongest bands was made in 1921 by Heger,[1] and that they originate from the interstellar medium (ISM) was reported by Merrill[2] in 1934. According to a recent spectral atlas, the number of reported DIBs exceeds over 500.[3,4] Polycyclic aromatic hydrocarbons (PAHs) are a class of very stable aromatic organic molecules made of fused benzenoid rings and hydrogen atoms. Molecules containing carbon, in their neutral and ionized forms, play an important role in the ISM due to the rich chemistry of carbon and its ability to form a large variety of complex molecular species involving the most abundant element hydrogen.[5] The PAH-DIB proposal has been put forward, more than two decades ago, until now not a single PAH molecule could be unambiguously assigned to a DIB despite consistent efforts made by stellar and laboratory spectroscopists. Such an assignment also requires theoretical data, and the latter studies are missing in the literature. The present effort is aimed toward such a study.

Earlier laboratory spectroscopic study of PAHs⁺ were carried out in the gas phase and inert gas matrix environments.[6−19] In addition to photoelectron spectroscopy data at low resolution, zero electron kinetic energy (ZEKE) and time-resolved photoelectron spectroscopy measurements at higher resolution now opened up the possibility of better comparison with the stellar measurements. In the recent past, detailed theoretical studies on the radical cation of naphthalene (Np⁺), anthracene (An⁺), tetracene (Tn⁺), pentacene (Pn⁺), hexacene (Hn⁺)[20−24]

and l-C_3H_2 neutral[25] were carried out in our group. The theoretical results on the structure and dynamics of these radical cations were compared with those recorded in the laboratory[7,26,27] and also stellar measurements.[28−30] The theoretical results showed good agreement with the recorded and observed data revealing evidence that the Np⁺ and An⁺ could be the potential DIB carriers.[7,26,28]

Following our earlier work on PAH⁺s, (Np⁺, An⁺, Tn⁺, Pn⁺, and Hn⁺), we here focus on the study of quantum chemistry and dynamics of compact polycyclic aromatic hydrocarbons, viz., radical cation of phenanthrene (Pnt⁺), pyrene (Py⁺) and acenaphthene (Acn⁺). Availability of a vast amount of laboratory[6−19] and stellar[14] spectroscopy data on these radical cations is the primary motivation behind this study. Apart from this, it appears interesting to understand the complex vibronic coupling in the electronic excited states[20−22,24,25,31] of these species.

Several experimental groups have reported the photoelectron spectra of mentioned PAHs, and the observed ionization potentials were compared with theoretically calculated molecular orbital energies.[32−36] It is noted that high-resolution gas-phase spectral studies such as matrix isolation measurements on these systems and also the data recorded by stellar spectroscopists are the major input to establish the PAH-DIB hypothesis. From the literature, these molecular cations are predicted to be the carrier of the DIBs. In the case of Pnt⁺,

$\tilde{X} \to \tilde{B}$ transition apparently results in the 8572 Å DIB. Studies on Py$^+$ over the past several decades revealed that $\tilde{X} \to \tilde{E}$ transition may not be the source of 4430 Å DIB; on the other hand, the substituted Py$^+$ or Py$^+$-like species may be a carrier of this DIB. Very recently, ZEKE and multiphoton ionization spectra of Py are recorded by Kong et al.[37] These authors examined the spectral progressions and pointed out the importance of vibronic coupling. Except for some electronic structure calculations,[38−44] a detailed theoretical study has not been carried out on these molecules until now. The observations noted above will be discussed in relation to the theoretical model developed here. In addition, the lifetime of the excited electronic states of Pnt$^+$, Py$^+$, and Acn$^+$ is also estimated. Their nonradiative decay mechanism and photostability is discussed.

II. THEORY AND COMPUTATION

A. Hamiltonian. Neutral Pnt, Py, and Acn molecules possess planar equilibrium structure of C_{2v}, D_{2h}, and C_{2v} point group symmetry, respectively, in their electronic ground state. Removal of an electron from the highest occupied molecular orbital (HOMO), HOMO-1, HOMO-2, and HOMO-3 of the respective neutral species results the electronic ground ($\tilde{X}$) and first three excited $\tilde{A}$, $\tilde{B}$, and $\tilde{C}$ states of their radical cation, respectively. Based on elementary symmetry selection rules and dimensionless normal displacement coordinates of the vibrational modes (Q), the coupled states diabatic Hamiltonian of the energetically lowest four electronic states of these radical cations can be written as[45]

$$\mathcal{H} = (\mathcal{T}_N + \mathcal{V}_0)\mathbf{1}_4 + \begin{pmatrix} W_{\tilde{X}} & W_{\tilde{X}-\tilde{A}} & W_{\tilde{X}-\tilde{B}} & W_{\tilde{X}-\tilde{C}} \\ & W_{\tilde{A}} & W_{\tilde{A}-\tilde{B}} & W_{\tilde{A}-\tilde{C}} \\ & & W_{\tilde{B}} & W_{\tilde{B}-\tilde{C}} \\ h.c & & & W_{\tilde{C}} \end{pmatrix} \quad (1)$$

In the above equations, $\mathbf{1}_4$ is a 4 × 4 unit matrix. The quantity $(\mathcal{T}_N + \mathcal{V}_0)$ is the unperturbed Hamiltonian of the reference ground electronic state of the neutral molecule. In the harmonic approximation, the kinetic ($\mathcal{T}_N$) and potential ($\mathcal{V}_0$) energies of this reference state are given by

$$\mathcal{T}_N = -\frac{1}{2} \sum_{i=1}^{n} \omega_i \frac{\partial^2}{\partial Q_i^2} \quad (2)$$

$$\mathcal{V}_0 = \frac{1}{2} \sum_{i=1}^{n} \omega_i Q_i^2 \quad (3)$$

In eq 1, the diagonal elements of the Hamiltonian matrix represent the diabatic energies of the given electronic state, and their coupling energies are given by the off-diagonal elements. Employing the standard vibronic coupling theory[45] and a Taylor series expansion around reference equilibrium geometry (at $\mathbf{Q} = 0$), the Hamiltonian matrix elements can be expressed as

$$W_j = E_0^{(j)} + \sum_{i \in a_g \text{ or } a_1} \kappa_i^{(j)} Q_i + \frac{1}{2} \sum_{i \in \text{all}} \gamma_i^{(j)} Q_i^2; \, j \in \tilde{X}, \tilde{A}, \tilde{B}, \text{ and } \tilde{C} \quad (4)$$

$$W_{j-k} = \sum_i \lambda_i^{(j-k)} Q_i \quad (5)$$

with $j-k \in \tilde{X}-\tilde{A}, \tilde{X}-\tilde{B}, \tilde{X}-\tilde{C}, \tilde{A}-\tilde{B}, \tilde{A}-\tilde{C}, \tilde{B}-\tilde{C}$. The quantity $E_0^{(j)}$ in eq 4 denotes the vertical ionization energy of the jth electronic state. The linear and quadratic coupling parameters are represented as $\kappa_i^{(j)}$ and $\gamma_i^{(j)}$, respectively. The quantity $\lambda_i^{(j-k)}$ describes the interstate coupling between electronic states j and k through symmetry allowed i^{th} vibrational mode. Evaluation of the coupling parameters of the above Hamiltonian employing the calculated ab initio electronic energy data is discussed below.

B. Electronic Structure and Nuclear Dynamics. The optimized equilibrium geometry of electronic ground state of neutral Pnt, Py, and Acn molecules is calculated at the B3LYP level of theory[46] employing the 6-311G* basis set. Harmonic frequencies (ω_i) and normal coordinates of the vibrational modes of the elctronic ground state are calculated at the same level of theory. All calculations are performed using Gaussian 03 suite of programs.[47] The optimized equilibrium structures of these molecules are shown in Figure 1.
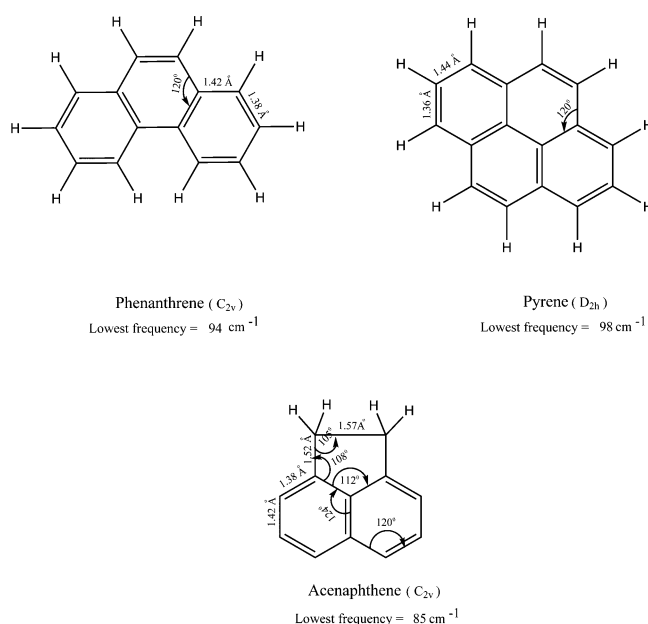
Figure 1. Otimized equilibrium structure of the electronic ground state of phenanthrene, pyrene, and acenaphthene.

The equilibrium symmetry representations of the normal vibrational modes of the mentioned molecules are given by

$$\text{Pnt}(C_{2v}): \Gamma_{\text{vib}} = 23a_1 + 11a_2 + 10b_1 + 22b_2 \quad (6)$$

$$\text{Py}(D_{2h}): \Gamma_{\text{vib}} = 13a_g + 5a_u + 4b_{1g} + 12b_{1u} + 7b_{2g}$$
$$+ 12b_{2u} + 12b_{3g} + 7b_{3u} \quad (7)$$

$$\text{Acn}(C_{2v}): \Gamma_{\text{vib}} = 20a_1 + 10a_2 + 11b_1 + 19b_2 \quad (8)$$

A quantum dynamical treatment of these large polyatomic systems including all electronic and nuclear degrees of freedom is extremely tedious. Therefore, in the following, electronic energies are calculated along all normal vibrational modes of each system. Thereafter, relevant vibrational modes are carefully chosen based on the Hamiltonian parameters extracted from the calculated electronic energy data. Finally, the constructed reduced dimensional Hamiltonian is employed for the nuclear dynamics study. The coupling parameters

Table 1. Linear (κ_i) and Quadratic (γ_i) Coupling Parameters of the Hamiltonian eq 1 of the $\tilde{X}$, $\tilde{A}$, $\tilde{B}$, and $\tilde{C}$ Electronic States of Pnt⁺, Py⁺, and Acn⁺ along the Totally Symmetric Vibrational Modes[a]

mode (frequency)	$\kappa_i^{(X)}$ ($\gamma_i^{(X)}$)	$\kappa_i^{(A)}$ ($\gamma_i^{(A)}$)	$\kappa_i^{(B)}$ ($\gamma_i^{(B)}$)	$\kappa_i^{(C)}$ ($\gamma_i^{(C)}$)
		Pnt⁺		
	$\tilde{X}^2B_1$	$\tilde{A}^2A_2$	$\tilde{B}^2A_2$	$\tilde{C}^2B_1$
$\nu_6(0.2064)$	0.1523 (−0.0099)	−0.1044 (−0.0052)	0.0406 (0.0073)	0.0104 (−0.0029)
$\nu_7(0.2045)$	−0.0043 (−0.0075)	0.0866 (−0.0036)	−0.0818 (0.0069)	0.0857 (0.0057)
$\nu_{10}(0.1805)$	−0.0591 (0.0052)	−0.0114 (0.0054)	0.0592 (0.0117)	0.0350 (0.0064)
$\nu_{11}(0.1707)$	0.0949 (0.0100)	0.0868 (0.0122)	0.0094 (0.0153)	−0.0274 (0.0107)
$\nu_{12}(0.1647)$	−0.0336 (0.0044)	0.0321 (0.0009)	0.0376 (0.0061)	−0.0692 (0.0050)
$\nu_{13}(0.1577)$	0.0538 (0.0011)	−0.0227 (0.0039)	0.0717 (0.0044)	−0.0516 (0.0012)
$\nu_{18}(0.1320)$	0.0050 (0.0016)	0.0320 (0.0021)	0.0259 (−0.0001)	0.0442 (−0.0001)
$\nu_{19}(0.1047)$	−0.0101 (−0.0008)	0.0022 (−0.0023)	−0.0524 (−0.0001)	0.0329 (−0.0001)
$\nu_{20}(0.0898)$	0.0023 (−0.0025)	0.0556 (−0.0027)	0.0036 (−0.0001)	0.0498 (−0.0001)
$\nu_{21}(0.0692)$	0.0482 (−0.0021)	−0.0401 (−0.0013)	−0.0126 (−0.0007)	−0.0462 (0.0001)
$\nu_{22}(0.0511)$	0.0253 (0.0002)	−0.0484 (−0.0018)	0.0278 (−0.00004)	0.0226 (−0.0014)
$\nu_{23}(0.0309)$	0.0199 (−0.0010)	−0.0206 (−0.0020)	0.0072 (−0.0027)	−0.0003 (−0.0022)
VIE	7.607	7.873	8.914	9.598
		Py⁺		
	$\tilde{X}^2B_{1g}$	$\tilde{A}^2B_{2g}$	$\tilde{B}^2B_{3u}$	$\tilde{C}^2A_u$
$\nu_4(0.2076)$	0.1509 (0.0043)	−0.1219 (−0.0018)	0.1212 (0.0022)	0.0380 (0.0011)
$\nu_5(0.1986)$	−0.0042 (−0.0005)	0.0703 (−0.0027)	0.0646 (0.0017)	−0.0937 (0.0030)
$\nu_6(0.1771)$	−0.0670 (−0.0003)	−0.0677 (0.0023)	0.0033 (0.0061)	0.0203 (0.0010)
$\nu_7(0.1680)$	0.0117 (0.0010)	−0.0106 (0.0042)	−0.0970 (−0.0027)	0.1019 (0.0026)
$\nu_8(0.1569)$	0.1064 (−0.0004)	0.0179 (0.0068)	−0.0250 (0.0070)	0.0287 (0.0048)
$\nu_{10}(0.1356)$	−0.0123 (0.0002)	−0.0479 (0.0021)	0.0273 (0.0016)	−0.0121 (0.0001)
$\nu_{11}(0.1012)$	0.0160 (0.0001)	−0.0306 (−0.0019)	−0.0508 (−0.0015)	0.0456 (−0.0008)
$\nu_{12}(0.0738)$	0.0194 (−0.0008)	−0.0509 (0.0009)	−0.0245 (−0.0010)	−0.0402 (0.0001)
$\nu_{13}(0.0511)$	−0.0216 (0.0010)	0.0639 (−0.0012)	−0.0597 (0.0001)	−0.0276 (−0.0006)
VIE	7.068	7.953	8.728	9.116
		Acn⁺		
	$\tilde{X}^2A_2$	$\tilde{A}^2B_1$	$\tilde{B}^2B_1$	$\tilde{C}^2A_2$
$\nu_5(0.2037)$	0.0930 (−0.0029)	−0.0437 (−0.0124)	0.0666 (0.0179)	0.0112 (0.0114)
$\nu_6(0.2034)$	−0.1012 (−0.0001)	0.1029 (0.0018)	−0.1186 (0.0129)	−0.0243 (0.0069)
$\nu_7(0.1873)$	−0.0393 (−0.0101)	0.0061 (−0.0005)	−0.0184 (−0.0092)	−0.0643 (−0.0247)
$\nu_8(0.1822)$	0.0978 (0.0036)	0.0221 (0.0009)	−0.0507 (0.0113)	0.1139 (0.0012)
$\nu_9(0.1803)$	0.0986 (0.0025)	−0.0191 (0.0116)	−0.0262 (0.0063)	0.0034 (0.0075)
$\nu_{10}(0.1732)$	−0.0953 (0.0025)	−0.0270 (0.0080)	0.0224 (0.0112)	−0.0207 (0.0047)
$\nu_{12}(0.1554)$	0.0406 (−0.0014)	0.0336 (0.0042)	0.0345 (0.0012)	0.0493 (−0.0035)
$\nu_{13}(0.1490)$	0.0466 (0.0036)	−0.0607 (0.0058)	0.0217 (0.0049)	−0.0094 (0.0066)
$\nu_{14}(0.1323)$	−0.0131 (−0.0004)	0.0670 (0.0041)	−0.0086 (0.0005)	0.1157 (0.0054)
$\nu_{15}(0.1258)$	0.0016 (−0.0027)	0.0496 (0.0001)	0.0391 (−0.0022)	0.0335 (−0.0009)
$\nu_{16}(0.1177)$	−0.0053 (−0.0010)	−0.0180(0.0010)	0.0051 (0.0017)	−0.0394 (−0.0027)
$\nu_{18}(0.0799)$	0.0047 (−0.0016)	−0.0376 (−0.0004)	−0.0509 (−0.0002)	−0.0326 (−0.0013)
$\nu_{19}(0.0686)$	−0.0150 (−0.0021)	0.0595 (−0.0003)	−0.0630 (−0.0009)	0.0065 (−0.0017)
$\nu_{20}(0.0525)$	0.0121 (−0.0037)	0.0331 (0.0001)	0.0445 (−0.0025)	−0.0041 (−0.0028)
VIE	7.405	8.341	9.368	10.595

[a]The VIEs of the above electronic states are also included in the table. All quantities are given in eV unit.

introduced in eqs 4 and 5 are the derivatives (of appropriate order) of adiabatic electronic energy with respect to $\mathbf{Q}$ evaluated at $\mathbf{Q} = 0$. The definition of these parameters is given elsewhere in the literature.[20−23,25]

The VIEs of the above molecules are calculated using outer-valence Green's function (OVGF) method[48] employing the 6-311G* basis set at various nuclear displacement along $\mathbf{Q}_i$ in the range $-4.0 \leq Q_i \leq +4.0$, using the Gaussian-03 program module.[47] These energies plus harmonic potentials are equated to the adiabatic functional form of the diabatic electronic Hamiltonian of eq 1 using a least-squares algorithm

$$\mathbf{S}^\dagger(\mathcal{H} - T_N \mathbf{1})\mathbf{S} = V \qquad (9)$$

and the parameters of the Hamiltonian are estimated. These parameters are given in Table 1−Table 3. In the latter, the parameters used in the following dynamics study are only given. Complete set of parameters for all three molecules along all vibrational modes are given in the online Supporting Information (Table SI).

The parametrized model Hamiltonian developed above is employed in the dynamics study, employing both time-independent and time-dependent quantum mechanical methods. Vibronic spectra of the electronic states and their internal

Table 2. Ab Initio Calculated Interstate Coupling Parameters of the Hamiltonian of Pnt$^+$, Py$^+$, and Acn$^+$ along the Relevant Coupling Vibrational Modes^a

Pnt$^+$

mode (frequency)	λ^{j-k}	λ^{j-k}	λ^{j-k}	λ^{j-k}
b_2	$j-k\in \tilde{X}-\tilde{A}$	$j-k\in \tilde{X}-\tilde{B}$	$j-k\in \tilde{A} - \tilde{C}$	$j-k\in \tilde{B} - \tilde{C}$
$\nu_{50}(0.2059)$	0.0409 (0.0197)	0.1158 (0.1581)	0.0923 (0.1005)	0.0226 (0.0060)
$\nu_{51}(0.1999)$	0.1044 (0.1364)	0.1054 (0.1390)	-	0.1009 (0.1274)
$\nu_{55}(0.1699)$	0.0660 (0.0754)	0.1010 (0.1767)	-	0.0189 (0.0062)
$\nu_{58}(0.1480)$	0.0462 (0.0487)	0.0671 (0.1028)	-	0.0243 (0.0135)
$\nu_{62}(0.1103)$	0.0259 (0.0275)	0.0485 (0.0967)	-	0.0154 (0.0097)
$\nu_{64}(0.0786)$	0.0323 (0.0844)	0.0326(0.0860)	-	0.0448 (0.1624)
$\nu_{65}(0.0628)$	0.0242 (0.0742)	0.0343 (0.1491)	0.0304 (0.1172)	0.0349 (0.1544)
$\nu_{66}(0.0554)$	0.0195 (0.0619)	0.0331 (0.1784)	-	0.0152 (0.0376)

Py$^+$

mode (frequency)	λ^{j-k}	λ^{j-k}	mode (frequency)	λ^{j-k}	λ^{j-k}	mode (frequency)	λ^{j-k}	λ^{j-k}
b_{1u}	$j-k\in \tilde{X}-\tilde{C}$	$j-k\in \tilde{A}-\tilde{B}$	b_{2u}	$j-k\in \tilde{X}-\tilde{B}$	$j-k\in \tilde{A}-\tilde{C}$	b_{3g}	$j-k\in \tilde{X}-\tilde{A}$	$j-k\in \tilde{B}-\tilde{C}$
$\nu_{26}(0.2033)$	0.1131 (0.1547)	0.0532 (0.0342)	$\nu_{44}(0.2046)$	0.0749 (0.0670)	0.0760 (0.0690)	$\nu_{56}(0.2019)$	0.1132 (0.1572)	0.0985 (0.1190)
$\nu_{27}(0.1845)$	-	0.0677 (0.0673)	$\nu_{45}(0.1884)$	0.1216 (0.2083)	-	$\nu_{59}(0.1738)$	0.0842 (0.1173)	0.0857 (0.1216)
$\nu_{29}(0.1578)$	0.0711 (0.1015)	0.0360 (0.0260)	$\nu_{52}(0.0688)$	0.0579 (0.3541)	0.0146 (0.0225)	$\nu_{64}(0.0632)$	0.0393 (0.1933)	0.0296 (0.1097)
$\nu_{32}(0.1037)$	0.0488 (0.1107)	0.0152 (0.0107)	$\nu_{53}(0.0446)$	0.0326 (0.2671)	-	$\nu_{65}(0.0574)$	0.0262 (0.1042)	0.0592 (0.5318)
$\nu_{33}(0.0874)$	-	0.0366 (0.0877)	-	-	-			

Acn$^+$

mode (frequency)	λ^{j-k}	λ^{j-k}	λ^{j-k}	λ^{j-k}
b_2	$j-k\in \tilde{X}-\tilde{A}$	$j-k\in \tilde{X}-\tilde{B}$	$j-k\in \tilde{A}-\tilde{C}$	$j-k\in \tilde{B}-\tilde{C}$
$\nu_{46}(0.2016)$	0.1522 (0.2727)	0.1527 (0.2745)	-	0.0095 (0.0011)
$\nu_{47}(0.1907)$	0.0444 (0.0271)	0.1068 (0.1568)	0.0948 (0.1236)	0.0195 (0.0052)
$\nu_{48}(0.1870)$	0.0328 (0.0154)	-	0.0824 (0.0971)	0.0809 (0.0936)
$\nu_{52}(0.1552)$	0.0345 (0.0247)	0.0568 (0.0670)	-	-
$\nu_{53}(0.1537)$	0.0185 (0.0072)	-	0.0586 (0.0727)	0.0508 (0.0546)
$\nu_{54}(0.1464)$	0.0581 (0.0787)	0.0294 (0.0202)	-	0.0530 (0.0655)
$\nu_{57}(0.1042)$	0.0260 (0.0311)	-	-	0.0330 (0.0501)
$\nu_{58}(0.0828)$	0.0308 (0.0692)	0.0453 (0.1496)	-	-
$\nu_{59}(0.0634)$	0.0603 (0.4523)	0.0587 (0.4286)	-	0.0219 (0.0596)
$\nu_{60}(0.0561)$	0.0193 (0.0592)	0.0252 (0.1009)	0.0038 (0.0023)	0.0077 (0.0094)

^{a}The symmetries of the vibrational modes are also given.

conversion dynamics are reported. Fermi's golden rule equation is used to calculate the vibronic spectrum. The spectral intensity is given by

$$P(E) = \sum_{v} |\langle \Psi_v^f|\hat{T}|\Psi_0^i\rangle|^2 \delta(E - E_v^f + E_0^i) \tag{10}$$

where $|\Psi_0^i\rangle$ is the initial state (reference) with energy E_0^i and $|\Psi_v^f\rangle$ is the final vibronic state with energy E_v^f. The initial reference state within the harmonic approximation is given by

$$|\Psi_0^i\rangle = |\Phi_0^0\rangle|0\rangle \tag{11}$$

where $|\Phi_0^0\rangle$ and $|0\rangle$ are the electronic and vibrational parts of the initial wave function, respectively. The transition dipole operator is given by $\hat{T}$ in eq 10.

The matrix Hamiltonian of eq 1 is represented in harmonic oscillator basis of the reference state and is diagonalized using the Lanczos algorithm[49] to calculate the stick vibronic spectrum.[20−23,25] This matrix diagonalization method is computationally very expensive to implement for systems with many electronic and vibrational degrees of freedom.

To circumvent this problem a time-dependent method is used to calculate the complete vibronic band structure of the coupled manifold of electronic states. The spectral intensity in this picture is given by

$$P(E) \approx 2Re \int_0^\infty e^{iEt/\hbar}\langle \Psi_f(0)|\tau^\dagger e^{-i\mathcal{H}t/\hbar}\tau|\Psi_f(0)\rangle dt \tag{12}$$

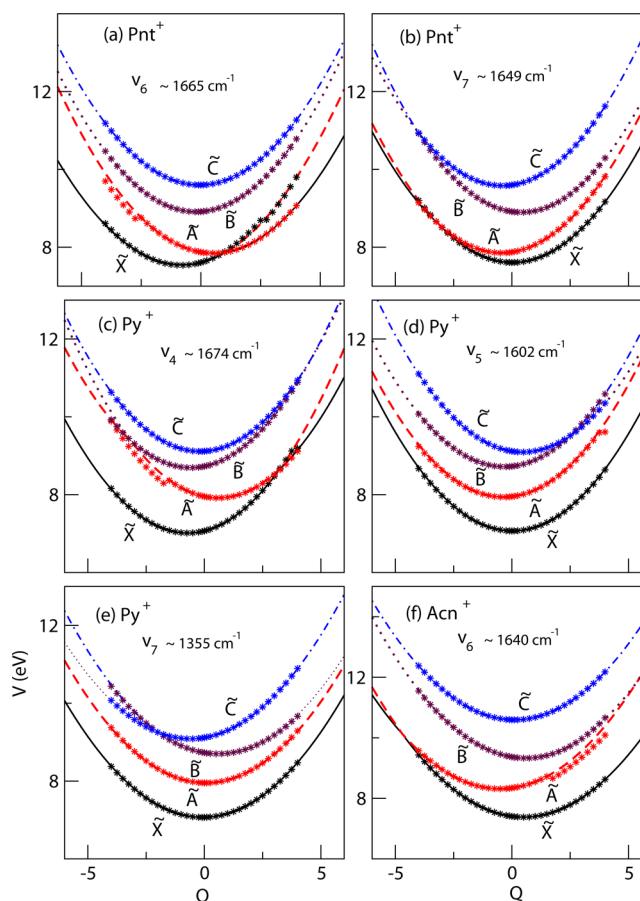$$\approx 2Re \int_0^\infty e^{iEt/\hbar} C_f(t)dt \tag{13}$$

where $\tau^\dagger = (\tau^{\tilde{X}}, \tau^{\tilde{A}}, \tau^{\tilde{B}}, \tau^{\tilde{C}})$ with $\tau^f = \langle \phi^f | \hat{T} | \phi^i\rangle$. The time-autocorrelation function of the wave packet (WP) in the fth electronic state of the radical cation is $C_f(t) = \langle \Psi_f(0) |\Psi_f(t)\rangle$ and $\Psi_f(t) = e^{-iHt/\hbar}\tau^f\Psi_i(0)$. The WP propagation approach within the multiconfiguration time-dependent Hartree (MCTDH) scheme is undertaken to calculate the broad band spectrum using eq 13. The efficient multiset ansatz of this method allows to combine multiple vibrational degrees of freedom into a single particle and efficiently reduces the dimensionality problem and computational overheads. For the details of the MCTDH method and its operational principles, the readers are referred to ref 50. The MCTDH suite of programs[50] developed in Heidelberg is used below to propagate WPs in the coupled electronic states. We include 20 vibrational modes out of 66 for Pnt$^+$, 22 out of 72 for Py$^+$, and 24 out of 60 for Acn$^+$. In order to justify the latter choice, we mention that the coupling parameters of the remaining vibrational modes in each case are small and do not affect the dynamical observables reported below.

Table 3. Ab Initio Calculated Quadratic Intrastate Coupling Parameters of the Hamiltonian of Pnt⁺, Py⁺, and Acn⁺ along the Relevant Coupling Vibrational Modes

mode	$\gamma_i^{(X)}$	$\gamma_i^{(A)}$	$\gamma_i^{(B)}$	$\gamma_i^{(C)}$
		Pnt⁺		
	$\tilde{X}^2B_1$	$\tilde{A}^2A_2$	$\tilde{B}^2A_2$	$\tilde{C}^2B_1$
$b_2\nu_{50}$	−0.0216	−0.0007	0.0148	0.0174
ν_{51}	−0.0379	0.0462	−0.0215	0.0262
ν_{55}	−0.0089	0.0392	0.0220	0.0243
ν_{58}	−0.0070	0.0172	0.0044	0.0079
ν_{62}	−0.0072	0.0020	−0.0004	0.0010
ν_{64}	−0.0097	0.0037	−0.0070	0.0041
ν_{65}	−0.0061	0.0018	−0.0028	0.0041
ν_{66}	−0.0044	0.0011	−0.0012	0.0003
		Py⁺		
	$\tilde{X}^2B_{1g}$	$\tilde{A}^2B_{2g}$	$\tilde{B}^2B_{3u}$	$\tilde{C}^2A_u$
$b_{1u}\nu_{26}$	−0.0079	−0.0138	−0.0001	0.0161
ν_{27}	−0.0009	−0.0101	0.0112	−0.0066
ν_{29}	−0.0018	−0.0014	0.0050	0.0078
ν_{32}	−0.0043	−0.0030	−0.0020	0.0002
ν_{33}	−0.0010	−0.0050	0.0016	−0.0023
$b_{2u}\nu_{44}$	−0.0112	−0.0081	0.0019	0.0106
ν_{45}	−0.0136	0.0051	0.0195	0.0008
ν_{52}	−0.0045	−0.0014	0.0034	−0.0007
ν_{53}	−0.0024	−0.0003	0.0001	−0.0020
$b_{3g}\nu_{56}$	−0.0239	0.0338	−0.0328	0.0290
ν_{59}	−0.0019	0.0380	−0.0212	0.0374
ν_{64}	−0.0040	0.0029	−0.0063	0.0020
ν_{65}	−0.0022	0.0009	−0.0154	0.0131
		Acn⁺		
	$\tilde{X}^2A_2$	$\tilde{A}^2B_1$	$\tilde{B}^2B_1$	$\tilde{C}^2A_2$
$b_2\nu_{46}$	−0.0346	0.0480	0.0035	0.0038
ν_{47}	−0.0118	−0.0040	0.0106	0.0119
ν_{48}	−0.0035	0.0010	−0.0074	0.0125
ν_{52}	0.0067	0.0118	0.0136	0.0032
ν_{53}	0.0001	0.0014	−0.0007	0.0074
ν_{54}	0.0046	0.0183	0.0064	0.0153
ν_{57}	−0.0028	0.0001	−0.0048	−0.0014
ν_{58}	−0.0035	0.0005	0.0008	−0.0003
ν_{59}	−0.0084	0.0064	−0.0015	−0.0001
ν_{60}	−0.0021	−0.0005	−0.0006	−0.0005

Figure 2. Adiabatic energies of the $\tilde{X}$, $\tilde{A}$, $\tilde{B}$, and $\tilde{C}$ electronic states of Pnt⁺ (panels a and b), Py⁺ (panels c, d, and e), and Acn⁺ (panel f) plotted along the dimensionless normal displacement coordinate of the vibrational mode indicated in the legend (see text for details). The electronic energies obtained from the present vibronic model and quantum chemistry calculations are shown by lines and points, respectively. For ready reference, the mode number and its harmonic frequency of the reference state is included in each panel.

III. RESULTS AND DISCUSSION

A. Potential Energy Surface of Ground and Excited Electronic States. In this section, the topography of the electronic states of Pnt⁺, Py⁺, and Acn⁺ is examined to evaluate the critical points like energetic minimum of conical intersections (CIs) and the equilibrium minimum of a state. These data are used to understand the quantum dynamics results shown and discussed in the following sections. The adiabatic PESs of the $\tilde{X}^2B_1$, $\tilde{A}^2A_2$, $\tilde{B}^2A_2$ and $\tilde{C}^2B_1$ electronic states of Pnt⁺; $\tilde{X}^2B_{1g}$, $\tilde{A}^2B_{2g}$, $\tilde{B}^2B_{3u}$, and $\tilde{C}^2A_u$ electronic states of Py⁺ and $\tilde{X}^2A_2$, $\tilde{A}^2B_1$, $\tilde{B}^2B_1$, and $\tilde{C}^2A_2$ electronic states of Acn⁺ are obtained by diagonalization of the respective diabatic electronic matrix of eq 1 with the parameters given in Table 1−Table 3. The adiabatic potential energy surfaces of $\tilde{X}$, $\tilde{A}$, $\tilde{B}$, and $\tilde{C}$ electronic states are plotted along the C═C stretching vibration and shown in Figure 2 for Pnt⁺ (panels a and b), Py⁺ (panel c, d, and e) and Acn⁺ (panel f). The calculated ab initio electronic energies and those obtained from the constructed vibronic model in Section II are plotted in each panel of Figure

2 and are shown by points and solid lines, respectively. The calculated ab initio energies can be seen to be well reproduced by the vibronic model developed here. We note that further higher level ab initio calculations could not be performed on these molecules. The small discontinuity in the ab initio energies seen in Figure 2 is likely to arise from the choice of ab initio method. Like in our previous studies on Np⁺, An⁺, Tn⁺, Pn⁺, and Hn⁺, low-energy CIs of electronic states appear along C═C stretching vibration in case of the present three cations. In Pnt⁺, quasi-degenerate inter-ring C═C stretching vibrations ν_6 and ν_7 (~1665 cm⁻¹ and ~1649 cm⁻¹, respectively) lead to crossing between its $\tilde{X}$ and $\tilde{A}$ electronic states. In Py⁺ three inter-ring C═C stretching vibrational modes ν_4, ν_5, and ν_7 (~1674, ~ 1602, and ~1355 cm⁻¹, respectively) are important. In this case, crossing between the $\tilde{B}$ and $\tilde{C}$ electronic states is caused by all these vibrational modes in addition to $\tilde{X}$−$\tilde{A}$ curve crossings (most prominent in case of ~1674 cm⁻¹ mode). Analogous to Pnt⁺, the former two vibrations are quasi-degenerate in this case also. In case of Acn⁺, only one C═C stretching vibrational mode ν_6 (~1640 cm⁻¹) causes $\tilde{X}$−$\tilde{A}$ and $\tilde{A}$−$\tilde{B}$ curve crossings but at larger displacements. These crossings develop into CIs of electronic PESs in multidimensions. It appears from the above observations that the

nonradiative internal conversion rate to the electronic ground state will be feasible for all three radical cations. This point is discussed latter in the text.

Various stationary points, viz., minimum energy of seam of various CIs and equilibrium minimum of a given state are calculated from the vibronic model. These stationary energy points are given in Table 4. The vertical energy gaps between

Table 4. Energetic Minimum of the Seam of Various Conical Intersections and the Estimated Equilibrium Minimum of a State Indicated in the Table

	Pnt^+	Py^+	Acn^+
states	intersection minimum (eV)		
$\tilde{X}-\tilde{A}$	7.73	8.70	8.44
$\tilde{X}-\tilde{B}$	10.74	11.71	13.11
$\tilde{X}-\tilde{C}$	11.91	15.40	23.53
$\tilde{A}-\tilde{B}$	9.33	8.71	9.49
$\tilde{A}-\tilde{C}$	12.46	9.66	18.59
$\tilde{B}-\tilde{C}$	9.66	9.05	11.40
state	equilibrium minimum (eV)		
$\tilde{A}$	7.72	7.81	8.21
$\tilde{B}$	8.83	8.60	9.23
$\tilde{C}$	9.49	9.02	10.46

$\tilde{X}-\tilde{A}$, $\tilde{A}-\tilde{B}$, and $\tilde{B}-\tilde{C}$ states are ~0.26, ~1.04, and ~0.68 eV; ~0.88, ~0.77, and ~0.39 eV; ~0.94, ~1.03, and ~1.23 eV (in that order) of Pnt^+, Py^+, and Acn^+, respectively. The data of Table 4 show that the energy gap between the minimum of $\tilde{A}$ and $\tilde{X}-\tilde{A}$ CIs of Pnt^+, Py^+, and Acn^+ is ~0.01, ~0.19, and ~0.23 eV, respectively. The energetic proximity of these two minima is likely to play crucial role in the nonradiative internal conversion dynamics. Like in case of noncompact PAH^+,[24] the spectroscopy of the $\tilde{B}$ state is also important here from the viewpoint of astrophysical observations. It can be seen from Table 4 that the minimum of the $\tilde{B}$ state occurs ~0.50, 0.11, and 0.26 eV below the $\tilde{A}-\tilde{B}$ intersection minimum in Pnt^+, Py^+, and Acn^+, respectively. Substantial broadening of the vibronic band structure of this state can therefore be expected in case of Py^+ and Acn^+.

B. Vibronic Structure of the Electronic Ground and Excited States vs Photoelectron Spectroscopy Measurements. In this section, a detailed study of the vibronic band structure of the $\tilde{X}$, $\tilde{A}$, $\tilde{B}$, and $\tilde{C}$ states of all three radical cations viz., Pnt^+, Py^+, and Acn^+ is presented and the findings are compared with the experimental low-resolution photoelectron spectroscopy data. The Hamiltonian parameters given in Table 1–Table 3 are used in the nuclear dynamics calculations in the coupled $\tilde{X}-\tilde{A}-\tilde{B}-\tilde{C}$ electronic states of Pnt^+, Py^+, and Acn^+. Based on coupling strength, only 20, 22, and 24 vibrational modes of Pnt^+, Py^+, and Acn^+, respectively, are found to be a relevant in the nuclear dynamics study.

Prior to time-dependent dynamics, reduced-dimensional calculations within a time-independent quantum mechanical approach are also performed to understand the vibronic structures of these radical cations. This task helps to identify and interpret progressions of various vibrational modes and their contributions in the broad band spectral envelope measured in the experiments.[32,34,36] The spectrum of the uncoupled state is calculated by the matrix diagonalization method discussed in Section II.A. The results are shown in panels a, b, and c of Figure 3 for Pnt^+, Py^+, and Acn^+,
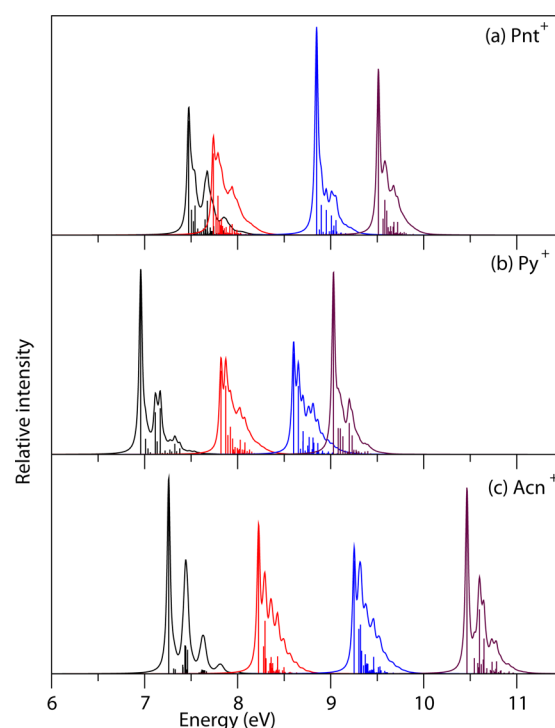
Figure 3. Uncoupled band structures of the $\tilde{X}$, $\tilde{A}$, $\tilde{B}$, and $\tilde{C}$ electronic states of Pnt^+ (panel a), Py^+ (panel b), and Acn^+ (panel c) calculated with the aid of the second-order vibronic Hamiltonian eq 1 and matrix diagonalization method.

respectively, in that order. The C=C stretching vibrations form the dominant progression in all three cases. In Pnt^+, peak spacings of ~0.030, ~0.051, ~0.068, ~0.176, and ~0.201 eV are obtained on the $\tilde{X}$ state and correspond to symmetric vibrational modes ν_{23}, ν_{22}, ν_{21}, ν_{11}, and ν_6, respectively. Peak spacings of ~0.030, ~0.050, ~0.068, ~0.088, ~0.177, ~0.203, and ~0.204 eV, corresponding to ν_{23}, ν_{22}, ν_{21}, ν_{20}, ν_{11}, ν_7, and ν_6 vibrational modes, respectively, are obtained in the $\tilde{A}$ state. The vibrational modes ν_{22}, ν_{19}, ν_{13} and ν_7 form major progressions in the $\tilde{B}$ state. The peaks are ~0.051, ~0.105, ~0.160, and ~0.208 eV spaced, respectively, in this state. In the $\tilde{C}$ state ν_{22}, ν_{21}, ν_{20}, ν_{12} and ν_7 vibrational modes form progressions with peak spacing of ~0.050, ~0.069, ~0.090, ~0.167 and ~0.207 eV, respectively.

The uncoupled state spectrum of Py^+ shown in panel b reveals peak spacings of ~0.052, ~0.157, ~0.177, and ~0.210 eV in the $\tilde{X}$ band. These are assigned to the vibrational modes ν_{13}, ν_8, ν_6, and ν_4, respectively. The vibrational modes ν_{13}, ν_{12}, and ν_4 are strongly excited in the $\tilde{A}$ state and peak spacings of ~0.050, ~0.074, and ~0.207 eV, respectively, are found in this case. Dominant progression of ν_{13}, ν_{11}, ν_7, and ν_4 vibrational modes is obtained in the $\tilde{B}$ state. The peaks are of ~0.051, ~0.100, ~0.167, and ~0.209 eV, respectively, spaced in this state. Peak spacings of ~0.051, ~0.074, ~0.101, ~0.169, and ~0.200 eV are found in the $\tilde{C}$ state and are assigned to the fundamentals of the ν_{13}, ν_{12}, ν_{11}, ν_7, and ν_5 vibrational modes, respectively.

For Acn^+ (panel c of Figure 3), the dominant peaks are ~0.174, ~0.182, ~0.184, ~0.202, and ~0.203 eV spaced in the $\tilde{X}$ state are assigned to ν_{10}, ν_9, ν_8, ν_5, and ν_6 vibrational modes, respectively. In the $\tilde{A}$ state the vibrational modes ν_{20}, ν_{19}, ν_{18}, ν_{14}, and ν_6 form progression and the peaks are ~0.053, ~0.068, ~0.080, ~0.134, and ~0.204 eV spaced, respectively.

Dominant progressions of ν_{20}, ν_{19}, ν_{18}, and ν_6 vibrations are found in the $\tilde{B}$ state. Peak spacings of ∼0.051, ∼ 0.068, ∼ 0.080, and ∼0.210 eV, respectively, are obtained. In the $\tilde{C}$ state peak spacings of ∼0.079, ∼ 0.135, and ∼0.183 eV are found and assigned to the excitation of ν_{18}, ν_{14}, and ν_8 vibrational modes, respectively. It is to be noted that the vibrational frequencies extracted from the peak spacings above correspond to their value at the reference state, modified by the second-order coupling parameter of the vibrational mode given in Table 1.

In the subsequent analysis, the coupling among the $\tilde{X}-\tilde{A}-\tilde{B}-\tilde{C}$ electronic states is included to understand the features observed in the recorded broad band vibronic spectra. Wave packet calculations are carried out employing the MCTDH method for this purpose. The initial WP is prepared in each electronic state of the radical cation separately and then propagated in the coupled electronic states. In each case, then WP is propagated for a total time of 200 fs. At each time step (1.0 fs), the autocorrelation function of the WP is recorded. The autocorrelation functions from separate calculations are combined, damped with an exponential function, e^{-t/τ_r} (with τ_r = 33 fs), and Fourier transformed to calculate the spectral envelope using eq 12. The numerical details of the converged MCTDH WP propagation are given in Table 5.

Table 5. Normal Mode Combinations and Size of the Primitive and Single-Particle Basis Used in the Converged WP Calculations using the MCTDH Algorithm in the Coupled $\tilde{X}$-$\tilde{A}$-$\tilde{B}$-$\tilde{C}$ Electronic States of Pnt$^+$, Py$^+$, and Acn$^+$

| normal modes	primitive basis	SPF basis
	Pnt$^+$	
(ν_{21}, ν_{18}, ν_{55}, ν_{66})	(14, 4, 10, 10)	[12, 8, 8, 10]
(ν_{65}, ν_{20}, ν_{50}, ν_{23})	(10, 12, 10, 14)	[10, 10, 8, 12]
(ν_{10}, ν_{12}, ν_{64}, ν_{22})	(4, 6, 10, 20)	[10, 8, 8, 12]
(ν_{19}, ν_{51}, ν_{13}, ν_6)	(8, 10, 8, 14)	[8, 10, 10, 12]
(ν_{62}, ν_{11}, ν_{58}, ν_7)	(8, 10, 8, 6)	[10, 8, 12, 10]
	Py$^+$	
(ν_{11}, ν_{26}, ν_{65}, ν_8)	(8, 8, 35, 15)	[14, 8, 12, 10]
(ν_{33}, ν_{10}, ν_{52}, ν_{64})	(6, 4, 16, 12)	[8, 14, 10, 12]
(ν_5, ν_{32}, ν_{12}, ν_{59})	(8, 6, 12, 6)	[12, 12, 14, 10]
(ν_7, ν_{53}, ν_{44}, ν_{29})	(10, 15, 4, 6)	[14, 8, 12, 10]
(ν_4, ν_{27}, ν_{13})	(14, 4, 30)	[8, 14, 10, 12]
(ν_6, ν_{45}, ν_{56})	(6, 12, 8)	[12, 14, 10, 8]
	Acn$^+$	
(ν_{18}, ν_7, ν_{57}, ν_{47})	(14 ,4, 4, 10)	[10, 8, 12, 8]
(ν_5, ν_{16}, ν_{53}, ν_{46})	(8, 4, 4, 14)	[12, 10, 8, 10]
(ν_9, ν_{12}, ν_{60}, ν_{19})	(10, 4, 6, 20)	[10, 12, 8, 10]
(ν_6, ν_{54}, ν_{48}, ν_{14})	(10, 4, 6, 18)	[8, 12, 10, 10]
(ν_{59}, ν_{10}, ν_{20}, ν_8)	(18, 10, 18, 10)	[10, 8, 10, 12]
(ν_{58}, ν_{15}, ν_{52}, ν_{13})	(10, 6, 4, 6)	[10, 12, 10, 8]

In Figure 4, the vibronic band structure of the coupled $\tilde{X}(1)-\tilde{A}(2)-\tilde{B}(3)-\tilde{C}(4)$ electronic states of Pnt$^+$ is presented. The calculated band structures and the experimental results reproduced from ref 34 are shown in panel a and b of this figure, respectively. It can be seen that the theoretical findings are in excellent agreement with the experiment. A detailed analysis of the vibronic band structure in Figure 4 reveals the following. The first band represents a composite structure of the $\tilde{X}(1)$ and $\tilde{A}(2)$ electronic states of Pnt$^+$. Figure 4 reveals that vibronic structure of these two states are highly overlapping. They are significantly different compared to their
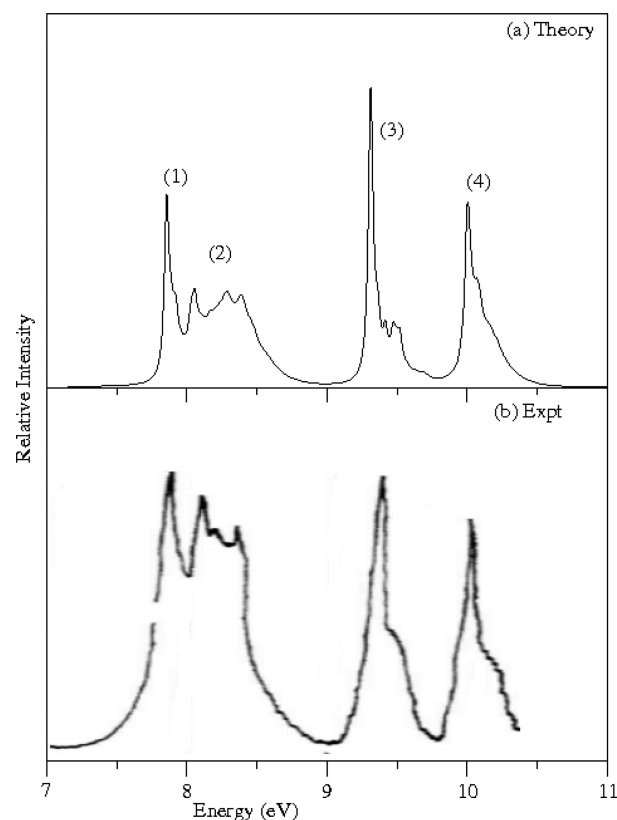
Figure 4. Vibronic structure of the coupled $\tilde{X}(1)-\tilde{A}(2)-\tilde{B}(3)-\tilde{C}(4)$ electronic states of Pnt$^+$. Relative intensity (in arbitrary units) is plotted as a function of the energy of the vibronic states of Pnt$^+$. The zero of the energy scale corresponds to the equilibrium minimum of the electronic ground state of the neutral reference. The present theoretical results are shown in panel a, and the experimental photoelectron spectroscopy results (reproduced from ref 34) are shown in panel b for comparison.

uncoupled state counterpart, as shown in Figure 3a. It is obvious from the discussion of Section IIIA and topography of the potential energy curves of Figure 2 that equilibrium minimum of these states are energetically very close to their intersection minimum. Because of this and strong coupling via b_2 vibrational modes [cf. Table 2], huge effects of nonadiabatic coupling show up in their vibronic band structure (1,2). We will return to this point later in the text. The structure of the $\tilde{B}$ and $\tilde{C}$ states (3 and 4) of Pnt$^+$ in the coupled states situation (cf. Figure 4) remains similar to that obtained in the uncoupled state situation (cf. Figure 3a). Weak perturbation in the coupled states vibronic structure arises due to coupling with the $\tilde{X}-\tilde{B}$, $\tilde{A}-\tilde{C}$, and $\tilde{B}-\tilde{C}$ states through vibrational modes of b_2 symmetry [cf. Table 2].

The vibronic spectrum of the coupled $\tilde{X}(1)-\tilde{A}(2)-\tilde{B}(3)-\tilde{C}(4)$ electronic states of Py$^+$ is shown in Figure 5. The theoretical results shown in panel a are in good accord with the experimental results of ref 32. shown in panel b. It is interesting to note that the vibronic structure of the $\tilde{X}$ state in Figure 5a remains essentially same as uncoupled state results shown in Figure 3b. Structure of the $\tilde{A}$ state in the coupled states calculations differs from the uncoupled state results. Broadening of the vibronic band structure in the coupled states situation (cf. Figure 5) arises due to coupling of the $\tilde{X}-\tilde{A}$, $\tilde{A}-\tilde{B}$, and $\tilde{A}-\tilde{C}$ states through vibrational modes of b_{3g}, b_{1u} and b_{2u} symmetry, respectively. The structure of the $\tilde{B}(2)-\tilde{C}(3)$ states
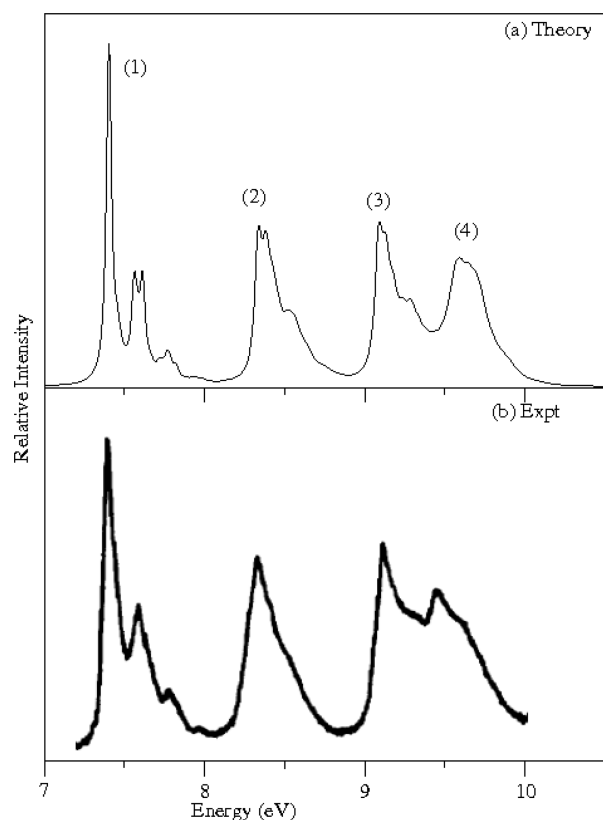
Figure 5. Same as in Figure 4 for the coupled $\tilde{X}(1)-\tilde{A}(2)-\tilde{B}(3)-\tilde{C}(4)$ electronic states of Py$^+$. The experimental results shown in panel b are reproduced from ref 32.

Figure 6. Same as in Figure 4 for the coupled $\tilde{X}(1)-\tilde{A}(2)-\tilde{B}(3)-\tilde{C}(4)$ electronic states of Acn$^+$. The experimental results shown in panel b are reproduced from ref 36.

is strongly affected by the vibronic coupling due to the vibrational modes of b_{3g} symmetry (cf. Table 2). It can be seen from Table 2 that coupling strengths of the b_{3g} modes are stronger between the $\tilde{B}$ and $\tilde{C}$ states of Py$^+$. Despite this, it follows from the discussion in Section IIIA that the energy gap between the minimum of $\tilde{B}-\tilde{C}$ crossing seam and the equilibrium minimum of the $\tilde{B}$ and $\tilde{C}$ states are very close in energy. The minimum of the $\tilde{B}-\tilde{C}$ intersection seam occurs ~0.45, ~ 0.03 eV above the minimum of $\tilde{B}$ and $\tilde{C}$ states, respectively. Therefore, the overall nonadiabatic effect is large in this case. Although, the $\tilde{A}-\tilde{B}$ coupling through vibrational modes of b$_{1u}$ symmetry (cf. Table 2) is relatively much weaker, the minimum of the $\tilde{B}$ state occurs only ~0.11 eV below the $\tilde{A}-\tilde{B}$ intersection minimum (cf. Table 5). Therefore, the $\tilde{A}-\tilde{B}$ coupling also contributes to the broadening of the low energy part of the vibronic band structure of the $\tilde{B}$ state of Py$^+$.

The final vibronic spectrum of the $\tilde{X}(1)-\tilde{A}(2)-\tilde{B}(3)-\tilde{C}(4)$ coupled electronic states of Acn$^+$ and the experimental spectrum reproduced from ref 36 are plotted in panel a and b of Figure 6, respectively. It can be seen from panel a that four discrete vibronic bands corresponding to four electronic states of Acn$^+$ are very similar to the uncoupled state results shown in Figure 3c. This shows that vibronic coupling effects in the energetically low-lying electronic states of Acn$^+$ are insignificant. This is in contrast to the situation in Pnt$^+$ and Py$^+$, for which overlapping band structures are obtained. This is due to the fact that the electronic states of Acn$^+$ are energetically well separated at the vertical configuration compared to those in Pnt$^+$ and Py$^+$. The $\tilde{B}-\tilde{C}$ coupling through vibrational mode of b$_2$ symmetry contributes to the broadening of the respective vibronic band structure in this case.
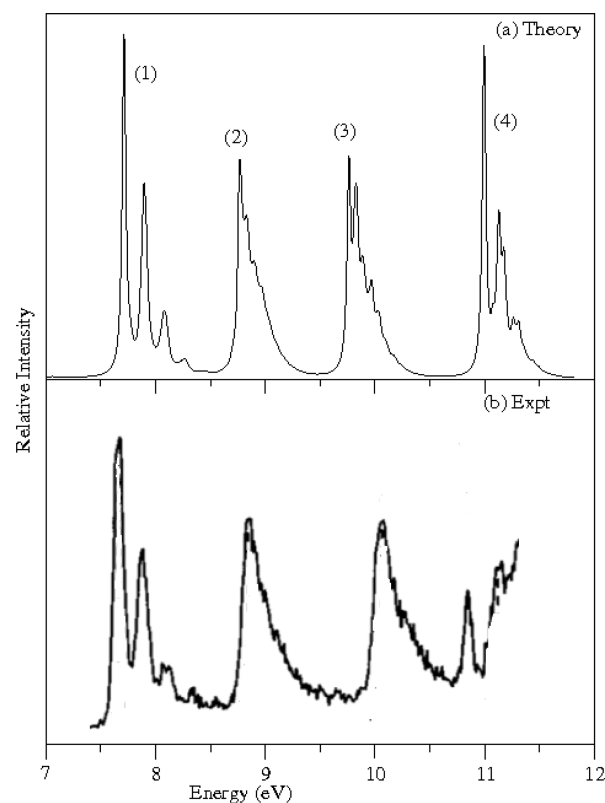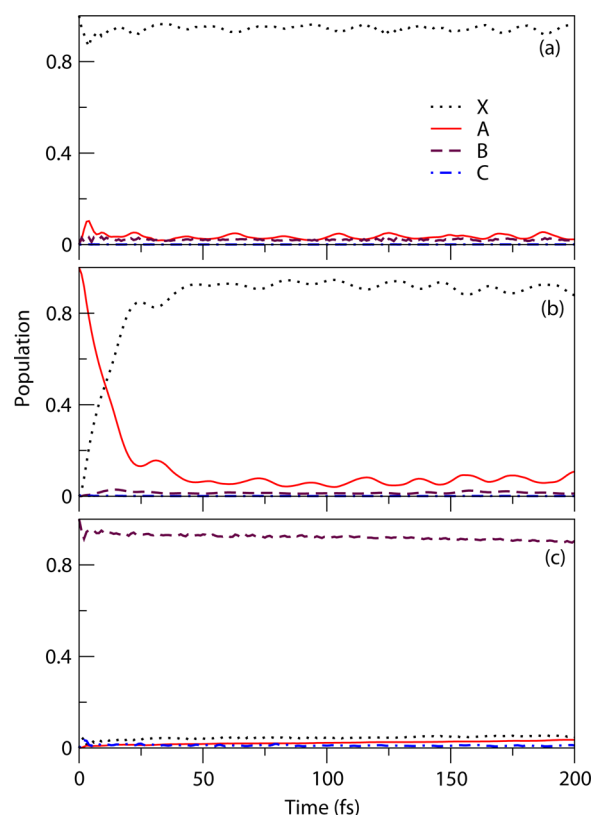
C. Time-Dependent Dynamics. Time-dependence of diabatic electronic populations in the $\tilde{X}-\tilde{A}-\tilde{B}-\tilde{C}$ coupled states dynamics of Pnt$^+$, Py$^+$, and Acn$^+$ is presented in Figure 7, Figure 8, and Figure 9, respectively. It is found that very little population moves to higher excited electronic states when the $\tilde{X}$ state is initially populated of all three radical cations (cf. panel a of Figure 7, Figure 8, and Figure 9). This is due to the fact that the $\tilde{X}$ state forms energetically inaccessible high energy CIs with all other states. The WP does not explore these intersections during its evolution on the $\tilde{X}$ state. The $\tilde{C}$ state may be coupled to further energetically higher electronic states, and an examination of those couplings is beyond the scope of present study. The population dynamics of the $\tilde{C}$ state is therefore not discussed here.

The population dynamics of the $\tilde{A}$ and $\tilde{B}$ electronic states of these radical cations is interesting and may be of astrophysical relevance. The time-dependence of electronic populations for an initial transition of the neutral molecule to the $\tilde{A}$ (panel b) and $\tilde{B}$ (panel c) ionic states are shown in Figure 7, Figure 8, and Figure 9 for Pnt$^+$, Py$^+$, and Acn$^+$, respectively. These populations are calculated by propagating WPs in the coupled $\tilde{X}-\tilde{A}-\tilde{B}-\tilde{C}$ electronic states in each case. It can be seen from these plots that the vibronic coupling monitors the nuclear dynamics in the $\tilde{A}$ and $\tilde{B}$ ionic states. The population decay of the $\tilde{A}$ state of all three cations is noteworthy. In the above figures, the populations of the $\tilde{X}$, $\tilde{A}$, $\tilde{B}$, and $\tilde{C}$ states are shown by the dotted, solid, dashed, and dot-dashed lines, respectively. The population flow to the $\tilde{X}$ state is quite large in case of all three molecular cations (panel b of Figure 7—Figure 9) when $\tilde{A}$ state is initially populated. In the case of Pnt$^+$, electron population rapidly moves to the $\tilde{X}$ state (~90% within 25 fs)
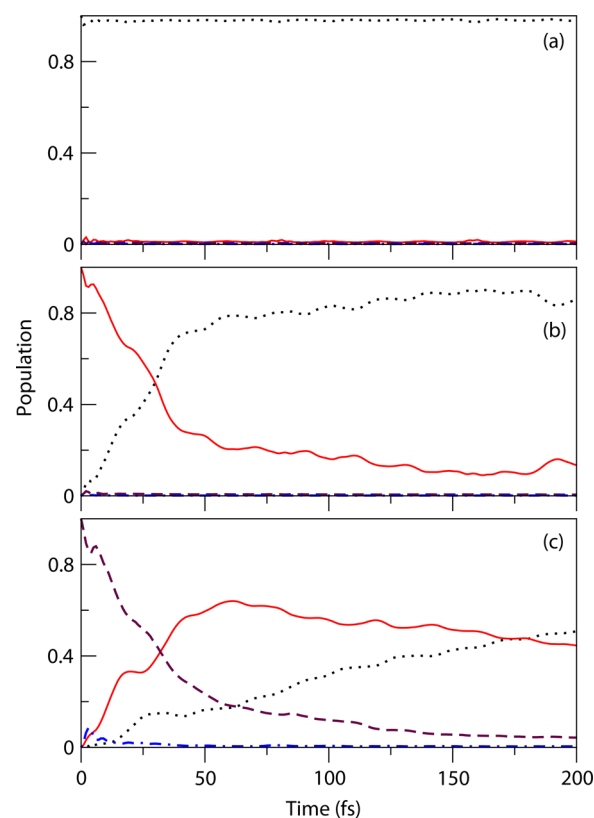
Figure 7. Time dependence of diabatic electronic populations for an initial transition of the WP to the $\tilde{X}$ (panel a), $\tilde{A}$ (panel b), $\tilde{B}$ (panel c) in the coupled $\tilde{X}-\tilde{A}-\tilde{B}-\tilde{C}$ state dynamics of Pnt$^+$. The line types of the population of each state is given in the legend.
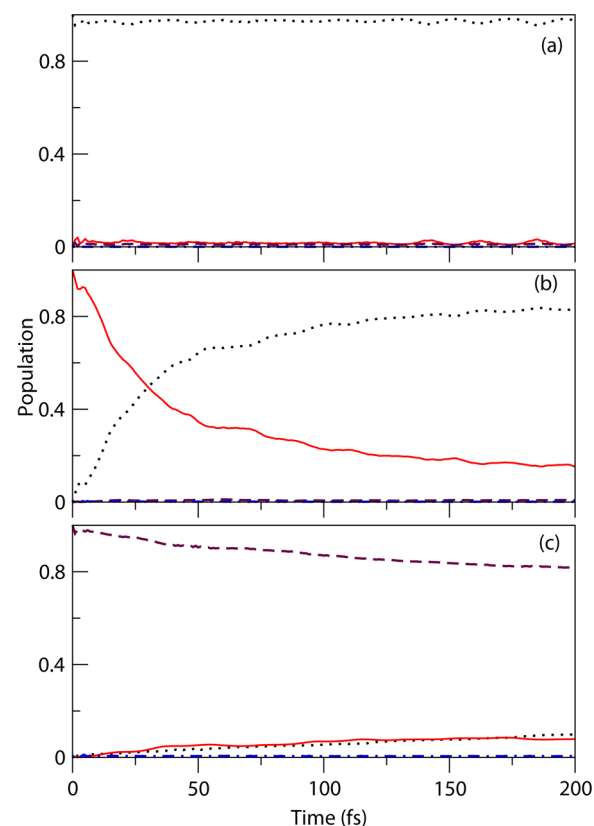
Figure 8. Same as in Figure 7, for the diabatic electronic populations of Py$^+$.

Figure 9. Same as in Figure 7, for the diabatic electronic populations of Acn$^+$.

when compared to the same for Py$^+$ and Acn$^+$. The location of the energetic minimum of the $\tilde{A}$ state relative to the minimum of the $\tilde{X}-\tilde{A}$ CIs drives the population dynamics. It follows from the discussion in Section III. A that the minimum of $\tilde{X}-\tilde{A}$ CIs progressively shifts to the higher energy relative to the $\tilde{A}$ state minimum from Pnt$^+$ to Py$^+$ to Acn$^+$. Because of this, relatively large fraction of population flows to the $\tilde{X}$ state of Pnt$^+$ despite moderate coupling strength of the b_2 vibrational modes (cf. Table 2). In contrast, coupling strength of b_{3g} vibrational modes is relatively stronger in the case of Py$^+$ (cf. Table 2); however, because of increasing energy gap between the $\tilde{X}-\tilde{A}$ intersection minimum and the minimum of the $\tilde{A}$ state (cf. Table 4), this coupling effect is quenched, and relatively less population flows to the $\tilde{X}$ state of Py$^+$ and Acn$^+$.

The data of Table 2 reveal that except $\tilde{X}-\tilde{C}$ and $\tilde{A}-\tilde{B}$ coupling in case of Pnt$^+$ and Acn$^+$, all other states of the three radical cations are linearly coupled. As a result, when the WP is propagated on the $\tilde{A}$ state no population flows to the $\tilde{B}$ state in case of Pnt$^+$ and Acn$^+$. Because of weaker $\tilde{A}-\tilde{B}$ coupling (cf. Table 2), very little population flows to the $\tilde{B}$ state of Py$^+$. The initial monotonic depletion of population relates to a decay rate of ~20, ~42, and ~52 fs of the $\tilde{A}$ state of Pnt$^+$, Py$^+$, and Acn$^+$, respectively.

The population dynamics seems to be more interesting and involved when the WP is initially prepared on the $\tilde{B}$ state. The population dynamics in this situation is shown in panel c of Figure 7, Figure 8, and Figure 9 for Pnt$^+$, Py$^+$, and Acn$^+$, respectively. As can be seen from the figures that large population transfer takes place to the $\tilde{X}$ and $\tilde{A}$ states of Py$^+$ in this situation (cf. panel c of Figure 8). The initial monotonic

depletion of population relates to a decay rate of ~37 fs, of the $\tilde{B}$ state of Py$^+$. As the $\tilde{A}-\tilde{B}$ coupling is absent in Pnt$^+$ and Acn$^+$, population transfer from $\tilde{B}$ state to the lower electronic states is very minor. It therefore follows from the above discussion that the nonradiative internal conversion probability to the electronic ground state decreases from Pnt$^+$ to Py$^+$ to Acn$^+$ for an initial excitation to the $\tilde{A}$ state. Therefore, the photostability of the latter state is greater in Pnt$^+$. In the case of initial excitation to the $\tilde{B}$ state, the internal conversion probability to the ground state is minimal in Pnt$^+$ and Acn$^+$. In contrast, this probability is quite large in the case of Py$^+$.

D. ZEKE Spectral Progression Comparison in Py$^+$. In this section, we compare the theoretically calculated vibrational energy levels of the $\tilde{X}$ state of Py$^+$ with the reported experimental ZEKE spectroscopy results within the 0−1520 cm^{-1} energy range.[37] The uncoupled $\tilde{X}$ state spectrum is calculated by the matrix diagonalization scheme using only low-frequency totally symmetric vibrational modes. From the theoretical data, observed peaks at ~416 and ~592 cm^{-1} are assigned to the fundamental of ν_{13} and ν_{12} vibrational modes, respectively. These fundamentals are found at 412 and 598 cm^{-1}, respectively, in the ZEKE spectroscopy results.[32,34,36] The first overtone of ν_{12} vibrational mode appears at ~1184 cm^{-1} and is consistent with an experimental ZEKE level at 1196 cm^{-1}. Peaks corresponding to combination modes $\nu_{13} + \nu_{12}$, $2\nu_{13} + \nu_{12}$ are also found at ~1008 and ~1424 cm^{-1}, respectively, and can be compared with the ZEKE spectroscopy results of 1010 and 1422 cm^{-1}, respectively.

Excitation of nontotally symmetric vibrational modes in the $\tilde{X}$ state spectrum can occur through its vibronic coupling with the other states. As discussed above in our theoretical model we find that $\tilde{X}-\tilde{C}$ and $\tilde{A}-\tilde{B}$ electronic states are coupled through the b_{1u} vibrational modes, $\tilde{X}-\tilde{B}$ and $\tilde{A}-\tilde{C}$ electronic states are coupled through the b_{2u} vibrational modes and $\tilde{X}-\tilde{A}$ and $\tilde{B}-\tilde{C}$ electronic states are coupled through the b_{3g} vibrational modes. In coupled states results, peak spacing at ~445, ~482, and ~751 cm^{-1} are assigned to the excitation of ν_{65}, ν_{64} and ν_{63} modes of b_{3g} symmetry. These findings compare very well with the ZEKE experimental findings of peaks at 457, 499 and 738, cm^{-1}. In addition to these fundamentals, combination bands $\nu_{12} + \nu_{65}$, $\nu_{12} + \nu_{64}$, $\nu_{12} + \nu_{63}$, and $\nu_{12} + \nu_{13} + \nu_{64}$ at ~1037, ~1074, ~1343, and ~1490 cm^{-1}, respectively, are found and are fully consistent with their ZEKE experimental locations reported at 1055, 1097, 1336, and 1509 cm^{-1}, respectively, in that order. Additional peaks, mostly the combinations associated with excitation of a_g, b_{1u}, b_{2u}, and b_{3g} modes, were also found in the $\tilde{X}-\tilde{A}-\tilde{B}-\tilde{C}$ coupled state calculation; however, an unambiguous assignment of these peaks seems difficult.

IV. SUMMARY AND OUTLOOK

Continuing with our earlier work on naphthalene, anthracene, tetracene, pentacene, and hexacene radical cations (abbreviated as Np$^+$, An$^+$, Tn$^+$, Pn$^+$, and Hn$^+$, respectively), in context of their relevance in stellar spectroscopy, in this paper we examined the spectroscopy and dynamics of phenanthrene, pyrene, and acenaphthene radical cations (of compact category). This work is pursued with the hope that the results may aid to confirm steller spectroscopy data on DIBs. The laboratory spectroscopy data are in perfect agreement with the theoretical results presented here. Energetically low-lying first four electronic states of these radical cations are considered in this study. Model vibronic Hamiltonian of the coupled manifold of $\tilde{X}-\tilde{A}-\tilde{B}-\tilde{C}$ electronic states are constructed in a

diabatic electronic basis. Standard vibronic coupling theory, symmetry selection rules and a Taylor expansion of the elements of the Hamiltonian is used in its construction. The parameters of the vibronic Hamiltonians are estimated through extensive calculation of adiabatic electronic energies of the four electronic states of each radical cation. First-principles nuclear dynamics calculations are carried out with the constructed Hamiltonians using time-independent and time-dependent quantum mechanical methods. The vibronic band structures of each electronic states are calculated and assigned. The impact of nonadiabatic coupling on them is discussed. The decay dynamics of each of the electronic states is also investigated. Theoretical results are compared with available experimental data. The topography of the adiabatic $\tilde{X}$, $\tilde{A}$, $\tilde{B}$, and $\tilde{C}$ electronic states of Pnt$^+$, Py$^+$, and Acn$^+$ is examined, and relevant stationary points on them are estimated. The nuclear dynamics on these states is examined in relation to their topographical features. Highly overlapping band structure of the $\tilde{X}$ and $\tilde{A}$ states of Pnt$^+$ follows from energetic proximity of their intersection seam and equilibrium minimum and the nonadiabatic coupling due to vibrational modes of b_2 symmetry. The nonradiative decay of the $\tilde{A}$ state predominantly populates the $\tilde{X}$ state of these radical cations. Decay rates of ~20, ~42, and ~52 fs of the diabatic $\tilde{A}$ state of Pnt$^+$, Py$^+$, and Acn$^+$, respectively, are estimated from the dynamics results. The spectroscopy and dynamics of the $\tilde{B}$ state of these radical cations seems to be important in stellar spectroscopy. Our findings here reveals that the dynamics of the $\tilde{B}$ state of Py$^+$ is mostly perturbed because of its coupling with the other states and close energetic location of its equilibrium minimum with respect to various intersection minimum. The latter occurs at high energies in case of Pnt$^+$ and Acn$^+$ and $\tilde{A}-\tilde{B}$ coupling is absent in these radical cations. Decay rate of ~37 fs is estimated from the population dynamics of the diabatic $\tilde{B}$ state of Py$^+$. In this case, despite weaker $\tilde{A}-\tilde{B}$ coupling, a significant fraction of the WP moves to the $\tilde{A}$ state because of energetic proximity of $\tilde{A}-\tilde{B}$ intersection and $\tilde{B}$ state minimum. Although $\tilde{B}$ state minimum is relatively far from $\tilde{X}-\tilde{B}$ intersection, because of strong $\tilde{X}-\tilde{B}$ coupling considerable population also flows to the $\tilde{X}$ state. Therefore, quantum yield of fluorescence of the $\tilde{B}$ state of Py$^+$ will be far lower than the corresponding state of Pnt$^+$ and Acn$^+$. Finally, the calculated vibronic level structure of the $\tilde{X}$ state of Py$^+$ is compared with the experimental ZEKE spectroscopy results. The calculated fundamentals of ν_{12} and ν_{13} symmetric vibrational modes at ~592 and ~416 cm^{-1}, respectively, compare well with their experimental location at ~598 and ~412 cm^{-1}. The first overtone of ν_{12} found at ~1184 cm^{-1} is observed at ~1196 cm^{-1} in the ZEKE results. Excitation of nontotally symmetric b_{3g} vibrational modes ν_{65}, ν_{64}, and ν_{63} found in the coupled states results at ~445, ~482, and ~751 cm^{-1}, respectively, is in good accord with their experimental location at ~457, ~499, and ~738 cm^{-1}. In addition to these, several combination levels of ν_{12} and ν_{13} and ν_{63}, ν_{64}, and ν_{65} are found to be in good accord with their experimental location. A detailed analysis of vibronic energy levels of the $\tilde{A}$ and $\tilde{B}$ electronic states of Np$^+$, An$^+$, Tn$^+$, Pn$^+$, Hn$^+$, Pnt$^+$, Py$^+$, and Acn$^+$ in relation to the available stellar spectroscopy data is currently underway.

■ ASSOCIATED CONTENT

Ⓢ Supporting Information

Complete set of parameters for all three molecules along all vibrational modes. The Supporting Information is available free

■ AUTHOR INFORMATION

Corresponding Author

*E-mail: susanta.mahapatra@uohyd.ac.in. Phone: +91-40-23134826.

Notes

The authors declare no competing financial interest.

■ DEDICATION

Dedicated to Professor Biman Bagchi on the occasion of his 60th birthday.

■ REFERENCES

(1) Heger, M. L. Future Study of the Sodium Lines in Class B Stars. *Lick Obs. Bull.* **1922**, *10*, 141−145.

(2) Merrill, P. W. Unidentified Interstellar Lines. *Publ. Astron. Soc. Pac.* **1934**, *46*, 206−207.

(3) Hobbs, L. M.; et al. A Catalog of Diffuse Interstellar Bands in the Spectrum of HD 204827. *Astrophys. J.* **2008**, *680*, 1256−1270.

(4) Hobbs, L. M.; et al. Studies of the Diffuse Interstellar Bands. III. HD 183143. *Astrophys. J.* **2009**, *70S*, 32−45.

(5) Salama, F. In *Organic Matter in Space, Proceedings of IAU Symposium 251*; Sandford, S., Kwok, S., Eds.; Cambridge University Press: Cambridge, 2008, p 357.

(6) Bréchignac, P.; Pino, T.; Boudin, N. Laboratory Spectra of Cold Gas Phase Polycyclic Aromatic Hydrocarbon Cations, and their Possible Relation to the Diffuse Interstellar Bands. *Spectrochim. Acta, Part A* **2001**, *57*, 745−756.

(7) Biennier, L.; Salama, F.; Allamandola, L. J.; Scherer, J. J. Pulsed Discharge Nozzle Cavity Ringdown Spectroscopy of Cold Polycyclic Aromatic Hydrocarbon Ions. *J. Chem. Phys.* **2003**, *118*, 7863−7872.

(8) Biennier, L.; Salama, F.; Gupta, M.; O'Keefe, A. Multiplex Integrated Cavity Output Spectroscopy of Cold PAH Cations. *Chem. Phys. Lett.* **2004**, *387*, 287−294.

(9) Bréchignac, P.; Pino, T. Electronic Spectra of Cold Gas Phase PAH cations: Towards the Identification of the Diffuse Interstellar Bands Carriers. *Astron. Astrophys.* **1999**, *343*, L49−L52.

(10) Tan, X.; Salama, F. Cavity Ring-Down Spectroscopy of Jet-Cooled 1-Pyrenecarboxyaldehyde ($C_{17}H_{10}O$) and 1-Methylpyrene ($C_{17}H_{12}$) Cations. *Chem. Phys. Lett.* **2006**, *422*, 518−521.

(11) Salama, F.; Allamandola, L. J. Is a Pyrene-Like Molecular Ion the Cause of THE 4430-Å Diffuse Interstellar Absorption Band. *Nature* **1992**, *358*, 42−43.

(12) Salama, F.; Joblin, C.; Allamandola, L. J. Electronic Absorption Spectroscopy of Matrix-Isolated Polycyclic Aromatic Hydrocarbon Cations. II. The Phenanthrene Cation ($C_{14}H_{10}^+$) and its 1-Methyl Derivative. *J. Chem. Phys.* **1994**, *101*, 10252−10262.

(13) Salama, F.; Joblin, C.; Allamandola, L. J. Neutral and Ionized PAHs: Contribution to the Interstellar Extinction. *Planet. Space Sci.* **1995**, *43*, 1165−1173.

(14) Salama, F.; Galazutdinov, G. A.; Krełowski, j.; Allamandola, L. J.; Musaev, F. A. Polycyclic Aromatic Hydrocarbons and the Diffuse Interstellar Bands: A Survey. *Astrophys. J.* **1999**, *526*, 265−273.

(15) Salama, F.; Allamandola, L. J. Neutral and Ionized Polycyclic Aromatic Hydrocarbons, Diffuse Interstellar Bands, and the Ultraviolet Extinction curve. *J. Chem. Soc., Faraday Trans.* **1993**, *89*, 2277−2284.

(16) Salama, F. The Diffuse Interstellar Bands: A Tracer for Organics in the Diffuse Interstellar Medium? *Origins Life Evol. Biospheres* **1998**, *28*, 349−364.

(17) Halasinski, T. M.; Salama, F.; Allamandola, L. J. Investigation of the Ultraviolet, Visible and Near-Infrared Absorption Spectra of Hydrogenated Polycyclic Aromatic Hydrocarbons and Their Cations. *Astrophys. J.* **2005**, *628*, 555−566.

(18) Salama, F.; Allamandola, L. J. Polycyclic Aromatic Hydrocarbon Ions and the Diffuse Interstellar Bands. *Adv. Space Res.* **1995**, *15*, 413−422.

(19) Crawford, K. M.; Tielens, M. G. G. A.; Allamandola, J. L. Ionized Polycyclic Aromatc Hydrocarbons and the Diffuse Interstellar Bands. *Astrophys. J.* **1985**, *293*, L45−L48.

(20) Reddy, V. S.; Mahapatra, S. Photostability of Electronically Excited Polyacenes: A Case Study of Vibronic Coupling in the Naphthalene Radical Cation. *J. Chem. Phys.* **2008**, *128*, 091104−091107.

(21) Reddy, V. S.; Ghanta, S.; Mahapatra, S. First Principles Quantum Dynamical Investigation Provides Evidence for the Role of Polycyclic Aromatic Hydrocarbon Radical Cations in Interstellar Physics. *Phys. Rev. Lett.* **2010**, *104*, 111102−111105.

(22) Ghanta, S.; Reddy, V. S.; Mahapatra, S. Theoretical Study of Electronically Excited Radical Cations of Naphthalene and Anthracene as Archetypal Models for Astrophysical Observations. I. Static Aspects. *Phys. Chem. Chem. Phys.* **2011**, *13*, 14523−14530.

(23) Ghanta, S.; Reddy, V. S.; Mahapatra, S. Theoretical Study of Electronically Excited Radical Cations of Naphthalene and Anthracene as Archetypal Models for Astrophysical Observations. II. Dynamical Consequences. *Phys. Chem. Chem. Phys.* **2011**, *13*, 14531−14541.

(24) Reddy, S. N.; Mahapatra, S. Theoretical Study on Molecules of Interstellar Interest. I. Radical Cation of Noncompact Polycyclic Aromatic Hydrocarbons. *J. Phys. Chem. A* **2013**, *117*, 8737−8749.

(25) Reddy, S. N.; Mahapatra, S. Theoretical Study of Electronic Absorption Spectroscopy of Propadienylidene Molecule vis-â-vis the Observed Diffuse Interstellar Bands. *Chem. Phys.* **2012**, *403*, 1−11.

(26) Sukhorukov, O.; Staicu, A.; Diegel, E.; Rouillé, G.; Henning, T.; Huisken, F. $D_2 \leftarrow D_0$ Transition of the Anthracene Cation Observed by Cavity Ring-Down Absorption Spectroscopy in a Supersonic Jet. *Chem. Phys. Lett.* **2004**, *386*, 259−264.

(27) Maier, J. P.; Walker, G. A. H.; Bohlender, D. A.; Mazzotti, F. J.; Raghunandan, R.; Fulara, J.; Garkusha, I.; Nagy, A. Identification of H_2CCC as a Diffuse Interstellar Band Carrier. *Astrophys. J.* **2011**, *726*, 41−49.

(28) Iglesias-Groth, S.; Manchado, A.; GarcÌa-Hernàndez, D. A.; Gonzàlez Hernàndez, J. I.; Lambert, D. L. Evidence for the Naphthalene Cation in a Region of the Interstellar Medium with Anomalous Microwave Emission. *Astrophys. J.* **2008**, *685*, L55−L58.

(29) Galazutdinov, G.; Lee, B.-C.; Song, I.-O.; Kazmierczak, M.; Krełowski, J. A Search for Interstellar Naphthalene and Anthracene Cations. *Mon. Not. R. Astron. Soc.* **2011**, *412*, 1259−1264.

(30) Krełowski, J.; Galazutdinov, G. A.; Kołos, R. Can H_2CCC be the Carrier of Broad Diffuse Bands? *Astrophys. J.* **2011**, *73S*, 124−129.

(31) Mahapatra, S. Excited Electronic States and Nonadiabatic Effects in Contemporary Chemical Dynamics. *Acc. Chem. Res.* **2009**, *42*, 1004−1015.

(32) Boschi, R.; Schmidt, W. Photoelectron Spectra of Polycyclic Aromatic Hydrocarbons. Pyrene and Coronene. *Tetrahedron Lett.* **1972**, *13*, 2577−2580.

(33) Schmidt, W. Photoelectron Spectra of Polynuclear Aromatics. V. Correlations with Ultraviolet Absorption Spectra in the Catacondensed Series. *J. Chem. Phys.* **1977**, *66*, 828−845.

(34) Boschi, R.; Murrell, J. N.; Schmidt, W. Photoelectron Spectra of Polycyclic Aromatic Hydrocarbons. *Faraday Discuss. Chem. Soc.* **1972**, *54*, 116−126.

(35) Hush, N. S.; Cheung, A. S.; Hilton, P. R. Binding Energies of π- and "Lone-Pair"-Levels in Mono- and Diaza-Phenanthrenes and Anthracenes: An He (I) Photoelectron Spectroscopic Study. *J. Electron Spectrosc. Relat. Phenom.* **1975**, *7*, 385−400.

(36) Bally, T.; Carra, C.; Fülscher, M. P.; Zhu, Z. Electronic Structure of the Naphthalene Radical Cation and Some Simple Alkylated Derivatives. *J. Chem. Soc., Perkin Trans. 2* **1998**, *2*, 1759−1765.

(37) Zhang, J.; Han, F.; Kong, W. Zero Kinetic Energy Photoelectron Spectroscopy of Pyrene. *J. Phys. Chem. A* **2010**, *114*, 11117−111124.

(38) Aiga, F. Theoretical Study on Oligoacenes and Polycyclic Aromatic Hydrocarbons Using the Restricted Active Space Self-Consistent Field Method. *J. Phys. Chem. A* **2012**, *116*, 663−669.

(39) Niederalt, C.; Grimme, S.; Peyerimhoff, S. D. Ab initio Theoretical Study of the Electronic Absorption Spectra of Polycyclic Aromatic Hydrocarbon Radical Cations of Naphthalene, Anthracene and Phenanthrene. *Chem. Phys. Lett.* **1995**, *245*, 455−462.

(40) Vala, M.; Szczepanski, J.; Pauzat, F.; Parisel, O.; Talbi, D.; Ellinger, Y. Electronic and Vibrational Spectra ofMatrix-Isolated Pyrene Radical Cations: Theoretical and Experimental Aspects. *J. Phys. Chem.* **1994**, *98*, 9187−9196.

(41) Deleuze, M. S. Valence One-Electron and Shake-Up Ionization Bands of Polycyclic Aromatic Hydrocarbons. II. Azulene, Phenanthrene, Pyrene, Chrysene, Triphenylene, and Perylene. *J. Chem. Phys.* **2002**, *116*, 7012−7026.

(42) Parisel, O.; Berthier, G.; Ellinger, Y. New Clues for Ionized Polycyclic Aromatic Hydrocarbons as Possible Carriers of Diffuse Interstellar Bands. *Astron. Astrophys.* **1992**, *266*, L1−L4.

(43) Tokmachev, A. M.; Boggio-Pasqua, M.; Bearpark, M. J.; Robb, M. A. Photostability via Sloped Conical Intersections: A Computational Study of the Pyrene Radical Cation. *J. Phys. Chem. A* **2008**, *112*, 10881−10886.

(44) Hirata, S.; Lee, T. J.; Head-Gordon, M. Time-Dependent Density Functional Study on the Electronic Excitation Energies of Polycyclic Aromatic Hydrocarbon Radical Cations of Naphthalene, Anthracene, Pyrene, and Perylene. *J. Chem. Phys.* **1999**, *111*, 8904−8912.

(45) Köppel, H.; Domcke, W.; Cederbaum, L. S. Multimode Molecular Dynamics Beyond the Born-Oppenheimer Approximation. In *Advances in Chemical Physics*; Prigogine, I., Rice, S. A., Eds; John Wiley & Sons, Inc.: Hoboken, NJ, 1984; Vol. 57, pp 59−246.

(46) Becke, A. D. Density-functional Thermochemistry. III. The Role of Exact Exchange. *J. Chem. Phys.* **1993**, *98*, 5648−5652.

(47) Frisch, M. J.; Trucks, G. W.; Schlegel, H. B. et al. *Gaussian 03*, Revision B.05, Gaussian, Inc.: Pittsburgh PA, 2003.

(48) Cederbaum, L. S. One-Body Green's Function for Atoms and Molecules: Theory and Application. *J. Phys. B: At. Mol. Phys.* **1975**, *8*, 290−303.

(49) Cullum, J.; Willoughby, R. *Lanczos Algorithms for Large Symmetric Eigenvalue Problems*; Birkhäuser: Boston, 1985; Vols. *I* and *II*.

(50) (a) Worth, G. A.; Beck, M. H.; Jäckle, A.; Meyer, H.-D. *The MCTDH Package*, Version 8.2; University of Heidelberg: Heidelberg, Germany, 2000. Meyer, H.-D. Version 8.3 (2002), Version 8.4 (2007). ML-MCTDH implemented in forthcoming version 8.5 (2011), see http://mctdh.uni-hd.de/. (b) Meyer, H.-D.; Manthe, U.; Cederbaum, L. S. The Multi- Configurational Time-Dependent Hartree Approach. *Chem. Phys. Lett.* **1990**, *165*, 73−78. (c) Manthe, U.; Meyer, H.-D.; Cederbaum, L. S. Wave-Packet Dynamics within the Multiconfiguration Hartree Framework: General Aspects and Application to NOCl. *J. Chem. Phys.* **1992**, *97*, 3199−3213. (d) Beck, M. H.; Jäckle, A.; Worth, G. A.; Meyer, H.-D. The Multiconfiguration Time-Dependent Hartree (MCTDH) Method: A Highly Efficient Algorithm for Propagating Wavepackets. *Phys. Rep.* **2000**, *324*, 1−105.